




# Nonthermal Emission from the Interaction of Magnetized Exoplanets with the Wind of Their Host Star

Xiawei Wang and Abraham Loeb 

Department of Astronomy, Harvard University, 60 Garden Street, Cambridge, MA 02138, USA

Received 2019 February 13; revised 2019 March 14; accepted 2019 March 18; published 2019 April 2

## Abstract

We study the nonthermal emission from the interaction between magnetized Jupiter-like exoplanets and the wind from their host star. The supersonic motion of planets through the wind forms a bow shock that accelerates electrons that produce nonthermal radiation across a broad wavelength range. We discuss three wind mass-loss rates:  $\dot{M}_w \sim 10^{-14}$ ,  $10^{-9}$ ,  $10^{-6} M_\odot \text{ yr}^{-1}$  corresponding to solar-type, T Tauri, and massive O/B-type stars, respectively. We find that the expected radio synchrotron emission from a Jupiter-like planet is detectable by the Jansky Very Large Array and the Square Kilometre Array at  $\sim 1$ – $10$  GHz out to a distance of  $\sim 100$  pc, whereas the infrared emission is detectable by the *James Webb Space Telescope* out to a similar distance. Inverse Compton scattering of the stellar radiation results in X-ray emission detectable by *Chandra* X-ray Observatory out to  $\sim 150$  pc. Finally, we apply our model to the upper limit constraints on V380 Tau, the first star–hot Jupiter system observed in radio wavelength. Our bow-shock model provides constraints on the magnetic field, the interplanetary medium, and the nonthermal emission efficiency in V380 Tau.

*Key words:* planet–star interactions – radio continuum: planetary systems – shock waves – stars: mass-loss

## 1. Introduction

Thousands of exoplanet systems have been identified over the past few decades (Winn & Fabrycky 2015). The majority of the currently known population was indirectly discovered via searches for the impact of the exoplanet on its host star.

In analogy with the solar system, exoplanets might possess intrinsic magnetic fields and generate nonthermal radio emission (Garraffo et al. 2016). These magnetized exoplanets can be probed in radio observations as they produce more radio emission than the host star. A number of observations support the existence of magnetic fields in exoplanets. For instance, the near-UV spectroscopic transit of a giant planet WASP-12b shows an early ingress compared to its optical transit and an excess absorption during the transit (Haswell et al. 2012); such a signature has been explained by absorption in a bow shock surrounding the planetary magnetosphere (Llama et al. 2011). Another clue is provided by the modulations of chromospheric spectral lines in phase with the orbital period, indicating induced activity on the stellar surface due to magnetic interactions between star and planet (Shkolnik et al. 2008). The magnetized planets in the solar system emit low-frequency radio waves from their auroral regions via the cyclotron maser instability (CMI; Treumann 2006). This emission is observed to be highly circularly (or elliptically) polarized and variable on a timescale from seconds to days (Treumann 2006; Zarka 2007). Magnetized exoplanets are expected to produce radio emission via a similar mechanism. The power of this emission can be estimated by the empirical relation known as the radiometric Bode’s law, which relates the incident energy flux of the stellar wind to the radio intensity of a planet, as inferred from observations of magnetized planets in the solar system (Zarka et al. 2001). This method was applied to hot Jupiters but no detection has been reported as of yet (Jardine & Collier Cameron 2008).

A number of theoretical studies computed the expected exoplanetary radio emission by applying the radiometric Bode’s law. They found that the power of the radio emission

depends on the planetary magnetic field and the kinetic energy flux of the stellar wind or coronal mass ejections (Grießmeier et al. 2011). Lazio et al. (2004) predicted that planets on tight orbits at distances of a few parsecs might produce milliJansky level emission at  $\sim 10$ – $1000$  MHz frequencies. It has been suggested that stars with winds carrying a larger mass-loss rate and velocities than the Sun are ideal targets for radio observations (Stevens 2005), highlighting close-in hot Jupiters around pre-main-sequence and post-main-sequence stars for radio selection (Vidotto & Donati 2017). Many observational campaigns have made efforts to detect radio emission from exoplanets. Some of them targeted nearby hot Jupiters (e.g., Bastian et al. 2000; O’Gorman et al. 2018), while others searched for radio emission at locations of known exoplanets from low-frequency sky surveys (e.g., Lazio et al. 2004; Murphy et al. 2015).

Planetary emission can be used to discover new planets or set constraints on the properties of the interplanetary medium around stars (Wood et al. 2005). The interaction between exoplanets and stellar winds leads to distinct observational signatures, such as stellar activity enhancement (Shkolnik et al. 2005), cometary tail structures (Rappaport et al. 2012), and charge transfer between wind protons and neutral hydrogen atoms (Kislyakova et al. 2014). These signatures provide constraints on the mass-loss rate and speed of the stellar wind as well as the planetary magnetic field. The formation of a bow shock from the interaction between stellar wind and exoplanetary magnetic field has been considered (e.g., Zarka 2007; Vidotto et al. 2015). However, previous discussions were limited to low-frequency radio emission from CMI, with no detailed calculation of the nonthermal emission produced by relativistic particles accelerated by the bow shock.

Here, we compute the nonthermal spectrum as a novel observational signature of exoplanets as they travel in the wind of their host star. The supersonic motion of a planet can produce multiwavelength emission detectable at a distance of up to hundreds of parsecs with current and upcoming

instrumentation. Aside from revealing new planets, any detection of such an emission can be used to set constraints on the properties of the interplanetary medium, wind mass-loss rate, and planetary magnetic field.

Our discussion is organized as follows. In Section 2, we characterize the properties of the planetary bow shocks. In Section 3, we compute the resulting nonthermal synchrotron and inverse Compton (IC) emission. In Section 4, we apply our model to the solar system and the V380 Tau system. Finally, in Section 5, we summarize our results and discuss observational implications.

## 2. Planetary Bow Shock

As an exoplanet orbits around its host star, it interacts with the wind outflowing from the star. For simplicity, we assume that the wind speed  $v_w \sim v_{\text{esc}}$ , where  $v_{\text{esc}} \sim (2GM_*/R_*)^{1/2}$  is the escape velocity from the star,  $G$  is the Newton's constant, and  $M_*$  and  $R_*$  are the mass and radius of the star, respectively. The orbits of planets at small separation from their host star are often circularized by tidal dissipation, and their Keplerian orbital velocity is given by  $v_k = (GM_*/R_{\text{orb}})^{1/2}$ , where  $R_{\text{orb}}$  is the orbital radius of the planet. Thus, the effective velocity of the planet relative to the interplanetary plasma is of order  $\Delta v \sim (v_w^2 + v_k^2)^{1/2}$  (Lynch et al. 2018). For simplicity, we adopt an isothermal profile for the stellar wind,  $\rho_w = \dot{M}_w / (4\pi v_w R_{\text{orb}}^2)$ , where  $\dot{M}_w$  is the stellar mass-loss rate (See et al. 2014). The magnetic field of exoplanets shields the stellar wind and deflects the interplanetary particles from reaching the planetary atmosphere. Assuming a dipolar planetary magnetic field, we obtain the magnetic field at the standoff radius,  $B_p = B_0 (R_p/R_{\text{so}})^3$ , where  $B_0$  is the magnetic field at the equator on the planet's surface ( $\sim$ half of the intensity at the magnetic pole) and  $R_p$  is the planet's radius.

The standoff radius,  $R_{\text{so}}$ , is estimated by balancing the total pressure of the stellar wind and the planet's magnetic pressure:

$$\rho_w \approx \frac{1}{2} \rho_w \Delta v^2 = \frac{B_p^2}{8\pi}. \quad (1)$$

The thermal pressure of the wind is assumed to be negligible compared with its ram pressure (Vidotto et al. 2015). Therefore, the Mach number of the bow shock is given by  $\mathcal{M} = \Delta v/c_s$ , where  $c_s = (\Gamma P_w/\rho_w)^{1/2}$  is the sound speed, with  $\Gamma \sim 1$  for an isothermal gas, and  $P_w$  is the wind thermal pressure. For  $M_* \sim M_\odot$ ,  $R_* \sim R_\odot$ , and wind temperature  $T_w \sim 10^6$  K, the Mach number  $\mathcal{M} \sim 10$ , where  $R_\odot$  is the solar radius, consistent with numerical simulations (Vidotto et al. 2015). Therefore, the orbits of close-in hot Jupiters are supersonic, leading to a bow shock with a Mach cone of opening angle  $\sim 1/\mathcal{M}$  in the direction of planet's relative motion that accelerates interplanetary electrons to relativistic energies, producing nonthermal emission.

## 3. Nonthermal Emission

Next, we calculate the nonthermal emission from the bow shock as the planet plunges through the stellar wind with  $\mathcal{M} \gg 1$ .

### 3.1. Synchrotron Emission

In analogy with the collisionless shocks around supernova remnants (Helder et al. 2012), the free electrons in the interplanetary medium are expected to be accelerated to relativistic energies via the Fermi acceleration mechanism. Their energy distribution can be described by a broken power law:

$$N(\gamma)d\gamma = N_0 \gamma^{-p} \left(1 + \frac{\gamma}{\gamma_b}\right)^{-1} \quad (\gamma_{\text{min}} \leq \gamma \leq \gamma_{\text{max}}), \quad (2)$$

where  $N_0$  and  $p$  are the normalization factor and power-law index of the electron density distribution, with  $\gamma_b$ ,  $\gamma_{\text{min}}$ , and  $\gamma_{\text{max}}$  being the break, minimum, and maximum Lorentz factors, respectively. The electron acceleration timescale is given by  $t_{\text{acc}} = \xi_{\text{acc}} R_L c/v_w^2$ , where  $\xi_{\text{acc}}$  is a dimensionless constant of unity (Blandford & Eichler 1987),  $R_L = \gamma m_e c^2/eB_p$  is the Larmor radius, and  $m_e$  is the electron mass. The maximum Lorentz factor,  $\gamma_{\text{max}}$ , is obtained by equating  $t_{\text{acc}}$  to the minimum between the dynamical timescale,  $t_{\text{dyn}} \sim R_{\text{so}}/v_w$ , and the cooling timescale,  $t_{\text{cool}} = 3m_e c/4(U_B + U_*)\sigma_T \gamma$ . Here,  $U_B = B_p^2/8\pi$  and  $U_* = L_*/(4\pi R_{\text{so}}^2 c)$  are the energy densities of the magnetic field and host star, respectively, and  $\sigma_T$  is the Thomson cross-section. For typical parameters, we find that  $t_{\text{acc}} \gg t_{\text{dyn}}$ , and so  $\gamma_{\text{max}}$  is mainly constrained by  $t_{\text{dyn}}$ . The break Lorentz factor,  $\gamma_b$ , can be obtained by equating  $t_{\text{dyn}}$  and  $t_{\text{cool}}$ , which yields  $\gamma_b = 3m_e c v_w / 4\sigma_T R_{\text{so}} (U_B + U_*)$ . We adopt  $\gamma_{\text{min}} \sim 1$  in the calculation. The power-law index of accelerated electrons,  $p$ , is related to the Mach number of the shock,  $\mathcal{M}$ , through (Drury 1983; Gargaté & Spitkovsky 2012)

$$p = \frac{r+2}{r-1}, \quad (3)$$

where  $r$  is the shock compression ratio, derived from the shock jump condition

$$r = \frac{(\Gamma+1)\mathcal{M}^2}{(\Gamma-1)\mathcal{M}^2+2}. \quad (4)$$

$p \sim 2-2.2$  is inferred from numerical simulations of strong shocks (Gargaté & Spitkovsky 2012). Numerical simulation and observations of supernova-driven shocks suggests that  $p \sim 2.1-2.5$  (Helder et al. 2012; Caprioli & Spitkovsky 2014). Here, we consider  $p$  as a free parameter in the calculation. We assume that a fraction of the kinetic energy of the stellar wind is converted to the total nonthermal luminosity

$$L_{\text{nt}} = \epsilon_{\text{nt}} L_{\text{kin}} \approx \frac{1}{2} \epsilon_{\text{nt}} \rho_w \Delta v^3 (\pi R_{\text{so}}^2), \quad (5)$$

where  $\epsilon_{\text{nt}}$  is the fraction of electrons accelerated to produce nonthermal radiation, which we leave as a free parameter in our model. For supernova remnants,  $\epsilon_{\text{nt}} \sim 5\%$  (Helder et al. 2012).

Next, we compute the synchrotron emission following the standard formula from Rybicki & Lightman (1979). The emission and absorption coefficients are given by

$$j_\nu^{\text{syn}} = c_1 B \int_{\gamma_{\text{min}}}^{\gamma_{\text{max}}} F\left(\frac{\nu}{c_1 B \gamma^2}\right) N(\gamma) d\gamma, \quad (6)$$

$$\alpha_\nu^{\text{syn}} = -c_2 B \frac{1}{\nu^2} \int_{\gamma_{\text{min}}}^{\gamma_{\text{max}}} \gamma^2 \frac{d}{d\gamma} \left[ \frac{N(\gamma)}{\gamma^2} \right] F \left( \frac{\nu}{c_1 B \gamma^2} \right) d\gamma, \quad (7)$$

where  $c_1 = \sqrt{2} e^3 / 4\pi m_e c^2$ ,  $c_2 = \sqrt{2} e^3 / 8\pi m_e^2 c^2$ ,  $F(x) \equiv x \int_x^\infty K_{5/3}(\xi) d\xi$ , and  $K_{5/3}(x)$  is the modified Bessel function of 5/3 order. The synchrotron emission peaks at a frequency of  $\nu_{\text{syn}} = 4.2 \times 10^{14} B_1 \gamma_4^2$  Hz, where  $B_1 = (B_p/1 \text{ G})$  and  $\gamma_4 = (\gamma/10^4)$ . The specific intensity of synchrotron emission can be obtained by the radiative transfer equation (Rybicki & Lightman 1979)

$$I_\nu = \frac{j_\nu^{\text{syn}}}{\alpha_\nu^{\text{syn}}} (1 - e^{-\tau_\nu}), \quad (8)$$

where  $\tau_\nu$  is the optical depth. The solid lines in Figure 1 show the synchrotron emission for three cases of  $\dot{M}_w$ , which corresponds to solar-type stars ( $\dot{M}_w \sim 10^{-14} M_\odot \text{ yr}^{-1}$ ), T Tauri-type stars with intermediate mass loss ( $\dot{M}_w \sim 10^{-9} M_\odot \text{ yr}^{-1}$ ), and massive O/B-type stars ( $\dot{M}_w \sim 10^{-6} M_\odot \text{ yr}^{-1}$ ). We apply our model to the nonthermal emission produced by the bow shock from Jupiter in the solar system to constrain our free parameters. For a solar wind of mass-loss rate  $\dot{M}_w = 3 \times 10^{-14} M_\odot \text{ yr}^{-1}$ ,  $R_{\text{orb}} \sim 5 \text{ au}$ , Jovian polar magnetic field  $B_{\text{Jup}} \sim 7 \text{ G}$ , we find that  $R_{\text{so}} \sim 40 R_{\text{jup}}$ ,  $\gamma_{\text{max}} \sim 100$ , consistent with the estimate from de Pater & Dunn (2003). The observed radio flux at 1.4 GHz from Jupiter is  $\sim 4\text{--}5 \text{ Jy}$  (de Pater & Dunn 2003; Zarka 2007), setting an upper limit on  $\epsilon_{\text{nt}} \lesssim 0.3$ , consistent with the value of  $\epsilon_{\text{nt}} \sim 5\%$  inferred in supernova remnants (Helder et al. 2012).

We find that for massive stars, radio synchrotron emission below  $\sim 10 \text{ GHz}$  is self-absorbed, and emission at  $\gtrsim 10 \text{ GHz}$  can be detected at a distance of  $\lesssim 300 \text{ pc}$  (see Table 1 for details). For intermediate-mass stars, synchrotron self-absorption takes place at  $\sim 1 \text{ GHz}$ , and radio emission at  $\gtrsim 1 \text{ GHz}$  is observable out to  $\sim 200 \text{ pc}$ . For solar-type stars, GHz emission is not affected by self-absorption. However, the low kinetic luminosity of the wind leads to weak nonthermal intensity and the detectability is limited to  $\lesssim 100 \text{ pc}$ .

### 3.2. IC Scattering

IC scattering of low-energy photons by the same electrons responsible for the synchrotron emission could produce high-energy radiation. The soft photons are provided by the photosphere of the host star as well as the synchrotron photons. The energy density of the stellar radiation field is  $U_* = L_*/(4\pi R_{\text{orb}}^2 c)$ . In comparison, the magnetic field has an energy density of  $U_B = B_p^2/8\pi$ . The ratio between synchrotron and IC power is equivalent to the ratio between magnetic and stellar radiation energy density, i.e.,  $P_{\text{syn}}/P_{\text{IC}} = U_B/U_* \approx 0.01 B_1^2 R_{\text{orb},-2}^2 L_{*,\odot}^{-1}$ , where  $R_{\text{orb},-2} = (R_{\text{orb}}/10^{-2} \text{ au})$ ,  $L_{*,\odot} = (L_*/L_\odot)$ ,  $L_\odot$  is the solar luminosity. Thus, we expect significant IC emission from close-in exoplanet systems, such as hot Jupiters. For simplicity, we approximate the spectral energy distribution of the stellar emission as a blackbody spectrum of temperature  $T_*$ . The specific intensity of a stellar spectrum can be written as

$$I_\nu = \frac{L_*}{4\pi R_{\text{orb}}^2 c} f_\nu(T_*), \quad (9)$$

where  $f_\nu$  is the normalized Planck function. The stellar luminosity–mass relationship can be expressed as  $L_* \propto M_*^\alpha$ ,

where  $\alpha \sim 2.3, 4.0, 3.5,$  and  $1.0$  for  $M_* < 0.43 M_\odot$ ,  $0.43 < M_*/M_\odot < 2.0$ ,  $2.0 < M_*/M_\odot < 20$ , and  $M_\odot > 50 M_\odot$ , respectively (Malkov 2007).

The IC scattering of stellar photons peaks at a frequency of  $\nu_{\text{IC}} \approx \gamma^2 \nu_* = 5.9 \times 10^{21} \gamma_4^2 T_{*,3} \text{ Hz}$ , where  $\gamma_4 = (\gamma/10^4)$  and  $T_{*,3} = (T_*/10^3 \text{ K})$ . The differential production rate of high-energy photons with energy  $\epsilon m_e c^2$  is given by (Coppi & Blandford 1990)

$$Q(\epsilon) = \int d\epsilon_0 n(\epsilon_0) \int d\gamma N(\gamma) K(\epsilon, \gamma, \epsilon_0), \quad (10)$$

where  $\epsilon_0 m_e c^2$  is the soft photon energy,  $\gamma m_e c^2$  is the electron energy, and  $n(\epsilon_0)$  is the number density of soft photons.  $K(\epsilon, \gamma, \epsilon_0)$  is the Compton kernel, expressed as

$$K(\epsilon, \gamma, \epsilon_0) = \frac{2\pi r_e^2 c}{\gamma^2 \epsilon_0} \left[ 2\kappa \ln \kappa + (1 + 2\kappa)(1 - \kappa) + \frac{(4\epsilon_0 \gamma \kappa)^2}{2(1 + 4\epsilon_0 \gamma \kappa)} (1 - \kappa) \right], \quad (11)$$

where  $\kappa = \epsilon/[4\epsilon_0 \gamma (\gamma - \epsilon)]$  and  $r_e = e^2/m_e c^2$  is the classical electron radius. The emissivity of IC scattering is given by

$$j_\nu^{\text{IC}} = \frac{h}{4\pi} \epsilon Q(\epsilon), \quad (12)$$

where  $h$  is Planck's constant.

The expected IC emission for three cases of  $\dot{M}_w$  is shown by the dashed lines in Figure 1. We find that the X-ray emission is detectable by the *Chandra* X-ray Observatory out to a distance of  $\sim 200 \text{ pc}$  for massive stars (see Table 1 for details). In particular, for solar-type stars, the total power in IC exceeds the synchrotron power. Thus, X-ray observations could detect close-in planets with  $R_{\text{orb}} \lesssim 5 R_*$ .

### 3.3. Detectability

Table 1 summarizes the detectability of our calculated nonthermal emission. For solar-type stars ( $\dot{M}_w = 10^{-14} M_\odot \text{ yr}^{-1}$ ), the predicted radio fluxes are detectable out to  $\lesssim 100 \text{ pc}$  with current and upcoming instrumentation. The emission at higher frequencies is too weak for detection. For T Tauri stars ( $\dot{M}_w = 10^{-9} M_\odot \text{ yr}^{-1}$ ), we expect radio detection out to  $\sim 150 \text{ pc}$ . For massive O/B-type stars, the emission is bright across all wavelengths from radio to X-rays and observable out to a distance of  $\sim 300 \text{ pc}$ . Note that synchrotron self-absorption is significant at GHz for massive stars and the spectrum peaks at  $\gtrsim 8 \text{ GHz}$  (see Figure 1). Thus, radio observation at higher frequencies is required to detect synchrotron emission from massive stars, in contrast to the CMI expected at low frequencies (Vidotto et al. 2010).

## 4. Application to V380 Tau

We apply our model to V380 Tau, a nonaccreting solar mass T Tauri star that hosts a hot Jupiter orbiting at a radius of  $0.057 \text{ au}$ , located at a distance of  $150 \text{ pc}$  (Donati et al. 2016). Very Large Array observations at a frequency of  $6 \text{ GHz}$  reveal a flux density  $919 \pm 26 \mu\text{Jy}$ , along with nondetections at two other epochs corresponding to limits of  $< 66$  and  $< 150 \mu\text{Jy}$  (Bower et al. 2016). In addition, Very Long Baseline Array observations show one detection and one nondetection at comparable sensitivity, which indicates that the emission might be transient

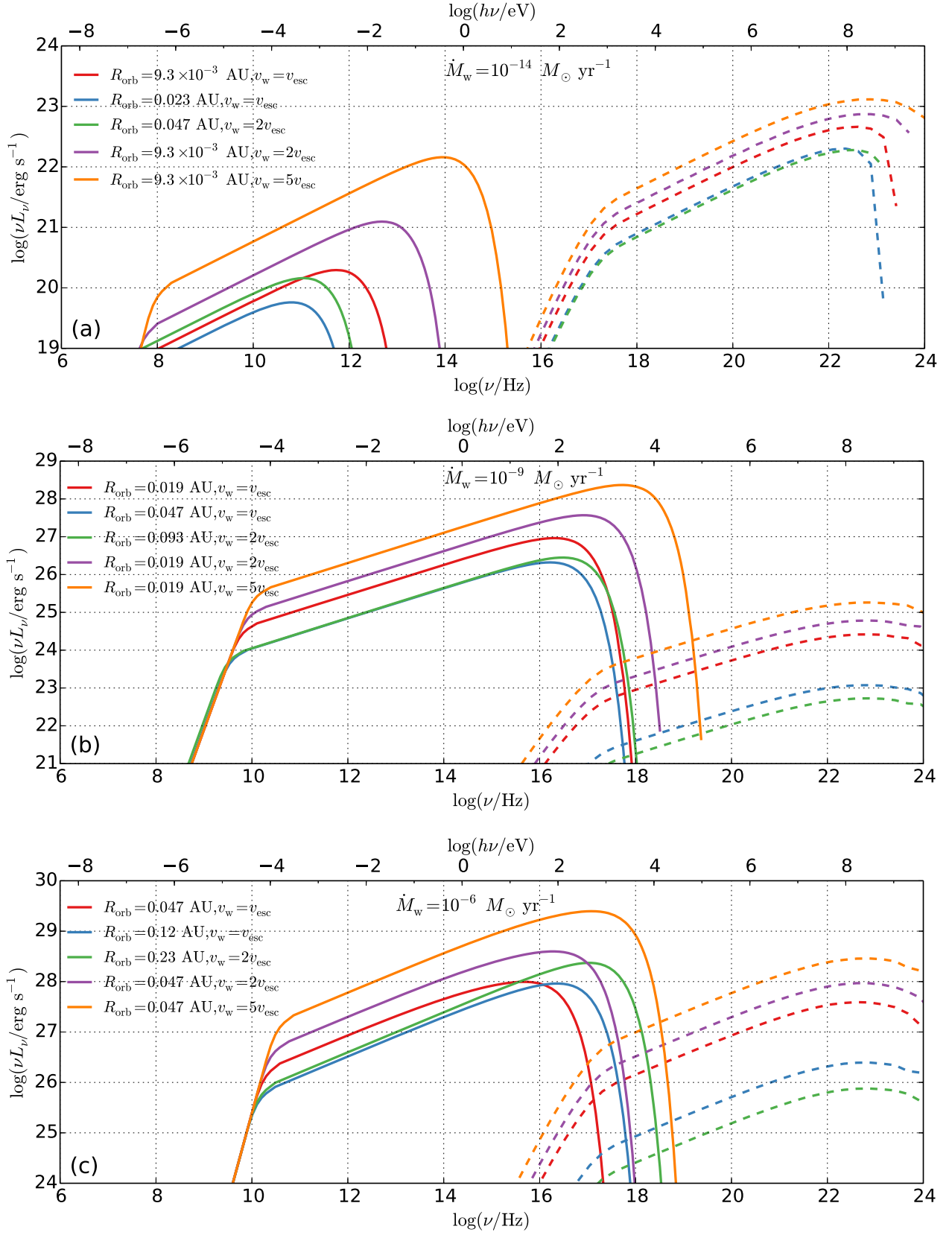


**Figure 1.** Nonthermal emission from stars with a characteristic wind mass-loss rate of  $\dot{M}_w \sim 10^{-14}$ ,  $10^{-9}$ , and  $10^{-6} M_\odot \text{ yr}^{-1}$ , interacting with Jupiter-like planets, as shown in panels (a)–(c), respectively. The solid and dashed lines correspond to synchrotron emission and inverse Compton scattering off stellar photons, respectively. The vertical axis shows the luminosity per  $e$ -folding in frequency, and the horizontal axes show the frequency in Hz (bottom) or the equivalent photon energy in eV (top). In panel (a),  $L_* \sim L_\odot$  and  $R_* \sim R_\odot$ . In panel (b),  $L_* \sim 3L_\odot$  and  $R_* \sim 2R_\odot$ . In panel (c),  $L_* \sim 10^3 L_\odot$  and  $R_* \sim 5R_\odot$ .

**Table 1**  
Detectability of Nonthermal Emission from Exoplanet Bow Shock at a Distance of 150 pc

Telescopes	$\dot{M}_w = 10^{-14} M_\odot \text{ yr}^{-1}$		$\dot{M}_w = 10^{-9} M_\odot \text{ yr}^{-1}$		$\dot{M}_w = 10^{-6} M_\odot \text{ yr}^{-1}$	
	$F_\nu$ ( $\mu\text{Jy}$ )	Detectability	$F_\nu$ ( $\mu\text{Jy}$ )	Detectability	$F_\nu$ ( $\mu\text{Jy}$ )	Detectability
JVLA	0.02; 0.004	No; No	0.2; 20	Marginal; Yes	0.3; 380	Marginal; Yes
SKA	0.02; 0.004	No	0.2; 20	Yes	0.3; 380	Yes
ALMA	0.001	No	4.0	Marginal	150	Yes
<i>HST</i>	N/A	No	0.038	Marginal	0.43	Yes
<i>JWST</i>	N/A	No	0.038	Marginal	0.43	Yes
	$\nu F_\nu$ ( $\text{erg cm}^{-2} \text{ s}^{-1}$ )	Detectability	$\nu F_\nu$ ( $\text{erg cm}^{-2} \text{ s}^{-1}$ )	Detectability	$\nu F_\nu$ ( $\text{erg cm}^{-2} \text{ s}^{-1}$ )	Detectability
<i>XMM-Newton</i>	$10^{-20}$	No	$4 \times 10^{-15}$	Yes	$1.9 \times 10^{-13}$	Yes
<i>ATHENA</i>	$10^{-20}$	No	$4 \times 10^{-15}$	Yes	$1.9 \times 10^{-13}$	Yes
<i>Chandra</i>	$2 \times 10^{-20}$	No	$5 \times 10^{-15}$	Yes	$4 \times 10^{-14}$	Yes
NuSTAR	$2 \times 10^{-20}$	No	$5 \times 10^{-15}$	Marginal	$4 \times 10^{-14}$	Yes

**Note.** We choose the characteristic values described in the text as representative examples for the exoplanet systems at a distance of  $\sim 150$  pc. For radio frequencies, we provide fluxes at 1 and 10 GHz, in units of mJy. For X-ray observation, we present  $\nu F_\nu$  in units of  $\text{erg cm}^{-2} \text{ s}^{-1}$ . The telescope detection limits are as follows: (1) *Jansky Very Large Array (JVLA)*:  $\sim 1 \mu\text{Jy}$  for  $1\sigma$  detection and 12 hr integration time at most bands (NRAO 2014). (2) *The Square Kilometer Array (SKA-MID)*:  $\sim 0.7 \mu\text{Jy}$  rms sensitivity for a 10 hr integration time (Prandoni & Seymour 2014). (3) *The Atacama Large Millimeter/submillimeter Array (ALMA)*: at frequency 345 GHz, the sensitivity  $\sim 8.7 \mu\text{Jy}$  for 10 hr integration time is calculated by the ALMA Sensitivity Calculator (ASC; <https://almascience.eso.org/proposing/sensitivity-calculator>). (4) *Hubble Space Telescope (HST)*: sensitivity  $\sim 40\text{--}50$  nJy for the wavelength range of  $0.6\text{--}1.5 \mu\text{m}$  for  $10\sigma$  detection and  $10^4$  s integration time (STScI 2013). (5) *The James Webb Space Telescope (JWST)*: sensitivity  $\sim 10$  nJy for the wavelength range of  $1\text{--}3 \mu\text{m}$  and  $\sim 30$  nJy for wavelengths  $4\text{--}5 \mu\text{m}$  for  $10\sigma$  detection and  $10^4$  s integration time (STScI 2013). (6) *Chandra*: sensitivity of high-resolution camera (HRC)  $\sim 9 \times 10^{-16} \text{ erg cm}^{-2} \text{ s}^{-1}$  covering energy range  $0.08\text{--}10$  keV for  $3\sigma$  detection and  $3 \times 10^5$  s integration time (CXC 2014). (7) *XMM-Newton*:  $\sim 3.1 \times 10^{-16} \text{ erg cm}^{-2} \text{ s}^{-1}$  in the  $0.5\text{--}2.0$  keV band (Hasinger et al. 2001). (8) *Advanced Telescope for High Energy Astrophysics (ATHENA)*:  $\sim 4 \times 10^{-17} \text{ erg cm}^{-2} \text{ s}^{-1}$  in the  $0.5\text{--}2$  keV band in a  $10^6$  s deep field (Barcons et al. 2012). (9) *Nuclear Spectroscopic Telescope Array (NuStar)*:  $\sim 2 \times 10^{-15} \text{ erg cm}^{-2} \text{ s}^{-1}$  in the  $6\text{--}10$  keV band for  $3\sigma$  detection and  $10^6$  s integration time (Harrison et al. 2013).

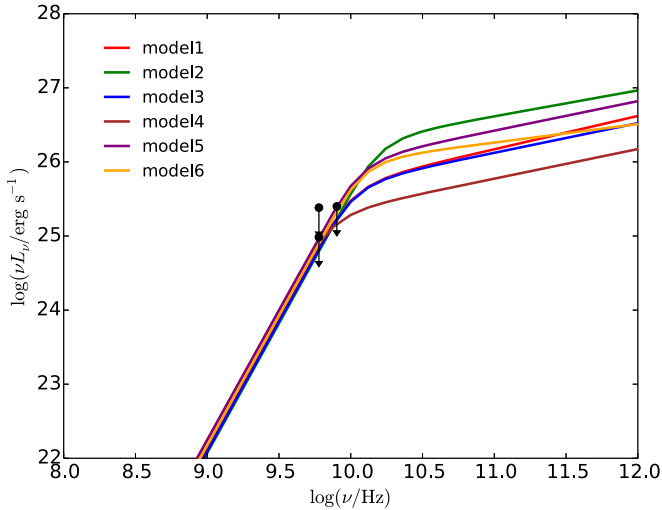


**Figure 2.** Estimated synchrotron emission from V380 Tau for the six models in Table 2. We estimate the nonthermal synchrotron emission from the interaction between stellar wind and magnetosphere of the hot Jupiter, constrained by nondetection upper limits from VLA and VLBA observations.

and possibly is nonthermal in origin (Bower et al. 2016). In Figure 2, we fit the nondetection limit of V380 Tau system using the bow-shock model with various combinations of parameters as listed in Table 2. We find that the synchrotron spectrum is steeper at  $\nu \lesssim 10$  GHz due to synchrotron self-absorption. An X-ray counterpart of this emission from IC emission is expected, as shown in Figure 1. Additionally, the predicted nonthermal synchrotron emission has a steeper spectrum than the CMI emission estimated from the radiometric Bode’s law (Vidotto & Donati 2017). The nonthermal

**Table 2**  
Model Parameters of Synchrotron Emission from V380 Tau

Parameters	$\dot{M}_w (M_\odot \text{ yr}^{-1})$	$\Delta v/v_{\text{esc}}$	$B_p$ (G)	$\epsilon_{\text{nt}}$	$p$
Model 1	$5 \times 10^{-9}$	6.0	2.0	0.1	2.1
Model 2	$5 \times 10^{-9}$	6.0	2.0	0.1	2.3
Model 3	$1 \times 10^{-8}$	2.0	2.0	0.1	2.2
Model 4	$6 \times 10^{-10}$	3.0	1.0	0.25	2.2
Model 5	$1 \times 10^{-8}$	1.0	1.0	0.25	2.2
Model 6	$1 \times 10^{-10}$	7.0	1.0	0.5	2.5

**Note.**  $\dot{M}_w$ : stellar wind mass-loss rate;  $\Delta v/v_{\text{esc}}$ : the ratio between an exoplanet’s relative speed to stellar wind and wind speed;  $\epsilon_{\text{nt}}$ : the fraction of wind kinetic luminosity converted to accelerate electrons to relativistic energies;  $p$ : the power-law index of nonthermal electrons;  $B_p$ : the magnetic field at the surface of the hot Jupiter.

emission model can be applied to CI Tau b, which is around a star of comparable age to V380 Tau (Johns-Krull et al. 2016).

## 5. Discussion

In this Letter, we studied the nonthermal emission produced by the supersonic motion of an exoplanet through the wind of its host stars. This produces a unique fingerprint of the interaction between the planet’s magnetosphere and the stellar wind, observable across a broad range of wavelengths from radio to X-rays. In particular, we considered three characteristic cases of stellar wind mass-loss rates, namely,  $\dot{M}_w = 10^{-14}, 10^{-9}, 10^{-6} M_\odot \text{ yr}^{-1}$ , corresponding to solar-type, T Tauri, and massive O/B stars, respectively. We have found that it is challenging to detect emission from solar-type stars farther than  $\sim 100$  pc, but the detection of planets around massive stars is feasible out to a distance of  $\sim 300$  pc. For stars

with an intermediate mass-loss rate, we find that X-ray frequencies allow the detection of exoplanets to a greater distance than their radio emission. For stars with substantial mass loss, the search for radio emission should be restricted to higher frequencies  $\gtrsim 10$  GHz as emission at lower frequencies is suppressed by synchrotron self-absorption. We note that the variability of the host star's magnetic field could mask the temporal variability from the bow shock (Llama et al. 2013).

Past observations have searched for radio signatures of cyclotron emission from close-in exoplanets at low radio frequency using instruments such as the Low Frequency Array (Zarka 2007). However, radio signatures of cyclotron emission from close-in exoplanets had not yet been detected due to instrumental sensitivity limitations at the  $\sim 100$  MHz frequency range (Bastian et al. 2000), though subtle hints of such emission had been claimed (e.g., O’Gorman et al. 2018), and it was postulated that the beaming of the emission could explain the nondetections (Lenc et al. 2018). As only a small fraction of the exoplanet orbits are sampled by these observations, there could be an optimal orbital phase for the related radio detection (Lynch et al. 2018). Weber et al. (2017) showed that supermassive planets such as Tau Bootis b and CI Tau b (Johns-Krull et al. 2016) are highly favorable targets for CMI emission. We find that the nonthermal signal is weakly subject to planet’s mass, making it more promising for detection of less massive planets than the CMI emission. Another CMI source is the host star itself, which could contaminate the emission from the planet (Llama et al. 2018; Cotton et al. 2019). However, the associated frequencies are  $\ll$  GHz, below the frequency of the nonthermal emission from planet–host star interaction. In addition to low-frequency CMI searches, we propose looking for the nonthermal signature of these systems at higher frequencies. Our calculations imply a new window for discovering exoplanet systems across a broad range of wavelengths from radio to X-rays. Detection of the emission signal from an exoplanet–wind interaction can provide constraints on the properties of stellar wind as well as the planet’s magnetosphere.

We thank an anonymous referee and John Forbes for insightful comments on the manuscript. This work was supported in part by a grant from the Breakthrough Prize Foundation.

### ORCID iDs

Abraham Loeb  <https://orcid.org/0000-0003-4330-287X>

### References

- Barcons, X., Barret, D., Decourchelle, A., et al. 2012, arXiv:1207.2745
- Bastian, T. S., Dulk, G. A., & Leblanc, Y. 2000, *ApJ*, **545**, 1058
- Blandford, R., & Eichler, D. 1987, *PhR*, **154**, 1
- Bower, G. C., Loinard, L., Dzib, S., et al. 2016, *ApJ*, **830**, 107
- Caprioli, D., & Spitkovsky, A. 2014, *ApJ*, **794**, 47
- Chandra X-Ray Center (CXC) 2014, The Chandra Proposers’ Observatory Guide Cycle 17.0, [http://cxc.harvard.edu/proposer/POG/arch\\_pdfs/](http://cxc.harvard.edu/proposer/POG/arch_pdfs/)
- Coppi, P. S., & Blandford, R. D. 1990, *MNRAS*, **245**, 453
- Cotton, D. V., Evensberger, D., Marsden, S. C., et al. 2019, *MNRAS*, **483**, 1574
- de Pater, I., & Dunn, D. E. 2003, *Icar*, **163**, 449
- Donati, J. F., Moutou, C., Malo, L., et al. 2016, *Natur*, **534**, 662
- Drury, L. O. 1983, *RPPh*, **46**, 973
- Gargaté, L., & Spitkovsky, A. 2012, *ApJ*, **744**, 67
- Garraffo, C., Drake, J. J., & Cohen, O. 2016, *ApJL*, **833**, L4
- Grieffmeier, J.-M., Zarka, P., & Girard, J. N. 2011, *RaSc*, **46**, RS0F09
- Harrison, F. A., Craig, W. W., Christensen, F. E., et al. 2013, *ApJ*, **770**, 103
- Hasinger, G., Altieri, B., Arnaud, M., et al. 2001, *A&A*, **365**, L45
- Kislyakova, K. G., Johnstone, C. P., Odert, P., et al. 2012, *ApJ*, **760**, 79
- Helder, E. A., Vink, J., Bykov, A. M., et al. 2012, *SSRv*, **173**, 369
- Jardine, M., & Collier Cameron, A. 2008, *A&A*, **490**, 843
- Johns-Krull, C. M., McLane, J. N., Prato, L., et al. 2016, *ApJ*, **826**, 206
- Haswell, C. A., Fossati, L., Ayres, T., et al. 2012, *ApJ*, **760**, 79
- Lazio, T. J. W., Farrell, W. M., & Dietrick, J. 2004, *ApJ*, **612**, 511
- Lenc, E., Murphy, T., Lynch, C. R., Kaplan, D. L., & Zhang, S. N. 2018, *MNRAS*, **478**, 2835
- Llama, J., Jardine, M. M., Wood, K., Hallinan, G., & Morin, J. 2018, *ApJ*, **854**, 7
- Llama, J., Vidotto, A. A., Jardine, M., et al. 2013, *MNRAS*, **436**, 2179
- Llama, J., Wood, K., Jardine, M., et al. 2011, *MNRAS*, **416**, L41
- Lynch, C. R., Murphy, T., Lenc, E., & Kaplan, D. L. 2018, *MNRAS*, **478**, 1763
- Malkov, O. Y. 2007, *MNRAS*, **382**, 1073
- Murphy, T., Bell, M. E., Kaplan, D. L., et al. 2015, *MNRAS*, **446**, 2560
- National Radio Astronomy Observatory (NRAO) website 2014, <http://www.science.nrao.edu/facilities/vla>
- O’Gorman, E., Coughlan, C. P., Vlemmings, W., et al. 2018, *A&A*, **612**, A52
- Prandoni, I., & Seymour, N. 2014, arXiv:1412.6942
- Puls, J., Vink, J. S., & Najarro, F. 2008, *A&ARv*, **16**, 209
- Rappaport, S., Levine, A., Chiang, E., et al. 2012, *ApJ*, **752**, 1
- Rybicki, G. B., & Lightman, A. P. 1979, *Radiative Processes in Astrophysics* (New York: Wiley-Interscience), 393
- See, V., Jardine, M., Vidotto, A. A., et al. 2014, *A&A*, **570**, A99
- Shkolnik, E., Bohlender, D. A., Walker, G. A. H., & Collier Cameron, A. 2008, *ApJ*, **676**, 628
- Shkolnik, E., Walker, G. A. H., Bohlender, D. A., Gu, P.-G., & Kürster, M. 2005, *ApJ*, **622**, 1075
- Space Telescope Science Institute (STScI) 2013, STScI Newsletter, Webb update, 30, 02
- Stevens, I. R. 2005, *MNRAS*, **356**, 1053
- Treumann, R. A. 2006, *A&ARv*, **13**, 229
- Vidotto, A. A., & Donati, J.-F. 2017, *A&A*, **602**, A39
- Vidotto, A. A., Fares, R., Jardine, M., Moutou, C., & Donati, J.-F. 2015, *MNRAS*, **449**, 4117
- Vidotto, A. A., Jardine, M., & Helling, C. 2010, *ApJL*, **722**, L168
- Wang, X., & Loeb, A. 2014, *MNRAS*, **441**, 809
- Weber, C., Lammer, H., Shaikhislamov, I. F., et al. 2017, *MNRAS*, **469**, 3505
- Winn, J. N., & Fabrycky, D. C. 2015, *ARA&A*, **53**, 409
- Wood, B. E., Müller, H.-R., Zank, G. P., Linsky, J. L., & Redfield, S. 2005, *ApJL*, **628**, L143
- Zarka, P. 2007, *P&SS*, **55**, 598
- Zarka, P., Treumann, R. A., Ryabov, B. P., & Ryabov, V. B. 2001, *Ap&SS*, **277**, 293